Atmospheric Phenomena

Table of Contents

Atmospheric Phenomena Introduction

Mesoscale and submesoscale atmospheric phenomena become visible on SAR images because they are associated with variations of the wind stress at the sea surface. The wind stress depends on the wind speed at the sea surface and on the stability of the air-sea interface which is a function of the temperature difference between water and air (Keller et al., 1989). When the water is warmer than the air, then the air-sea interface is unstable.

Variations of the wind speed at the sea surface disturb the small-scale sea surface roughness and thus give rise to "imprints" on the sea surface which are visible on the radar image as variations of the SAR image intensity.

From SAR images of the sea surface also quantitative information on the wind speed can be extracted. However, this is only possible when the wind direction is known. The wind direction can often be inferred from the SAR images itself, e.g., from the direction of the wind streaks or from the direction of the wind shadows behind mountainous island, or from weather charts. With this knowledge of the wind direction the wind speed can be extracted from the NRCS values by applying a wind scatterometer model like the CMOD4 model of ESA (Stoffelen et al., 1993) or the CMOD-IFR2 model of the Institut Français de Recherche pour l'Exploitation de la Mer (IFREMER) at Brest, France (Quilfen et al., 1993). Care has to be taken when converting ERS SAR image intensities into NRCS values because of nonlinearities in the ERS SAR analogue-to-digital converter (see Laur et al., 1997, Lehner et al, 1998). For a discussion of the accuracy of wind retrieval from ERS SAR images using the above mentioned C-band wind scatterometer models, the reader is referred to the papers of Vachon and Dobson (1996), Scoon et al. (1996), Furevik and Korsbakken (2000) and Horstmann et al. (2000).

The SAR onboard the ERS satellites, which operate at C-band and VV polarization, are much more sensitive for the detection of atmospheric phenomena in the marine boundary layer than the Seasat SAR, which operated at L-band and HH polarization. This is because the Bragg waves responsible for the radar backscattering at the sea surface have for ERS SAR a wavelength of 7 cm and for Seasat SAR a wavelength of 31 cm. Obviously, the 7 cm Bragg waves are much more responsive to wind variations than the 31 cm Bragg waves.

References

- Furevik, B.R. & Korsbakken, E., Comparison of derived wind speed from synthetic aperture radar and scatterometer during the ERS tandem phase, *IEEE Trans. Geoscience and Remote Sensing*, 2000, **38**, 1113-1121.
- Horstmann, J., Lehner, S., Koch, W. & Tonboe R., Computation of wind vectors over the ocean using spaceborne synthetic aperture radar, *Johns Hopkins APL Technical Digest*, 2000, **21** No.1, 100-107.
- Keller, W.C., Wismann, V. & Alpers, W., Tower-based measurements of the ocean C bnd radar backscattering cross section, *J. Geophys. Res.*, 1989, **94**, 924-930.
- Laur, H., Bally, P., Meadows, P., Sanchez, J., Schaettler, B. & Lopinto, E., ERS SAR calibration. Derivation of the backscattering coefficient σ^0 , ESA/ESRIN, Frascati, Italy. ESA ERS SAR PRI products, Tech. Rep. ES-TN-RS-PM-HL09.4, May 5 (1997).
- Lehner, S., Horstmann, J., Koch, W. & Rosenthal, W., Mesoscale wind measurements using recalibrated ERS SAR images, *J. Geophys. Res.*,1998, **103**, 7847-7856.
- Long, A.E., Towards a C-band radar sea echo model for the ERS-1 scatterometer, Proceedings of a conference on spectral signatures, Les Arc, France, *Eur. Space Agency Spec. Publ.*, 1985, ESA SP-247, 29-34.
- Quilfen, Y., Chapron, B., Elfouhaily, T., Katsaros, K. & Tournadre, J., Observation of tropical cyclones by high-resolution scatterometry, *J. Geophys. Res.*, 1998, **103**, 7767-7786.
- Scoon, A., Robinson, I.S. & Meadows, P.J., Demonstration of an improved calibration scheme for ERS-1 SAR imagery using a scatterometer wind model, *Int. J. Remote Sensing*, 1996, **17**, 413-418.
- Stoffelen, A. & Anderson, D., Scatterometer data interpretation: Estimation and validation of the transfer function CMOD4, *J. Geophys. Res.*, 1997, **102**, 5767-5780.

Atmospheric Gravity Waves

Introduction

Atmospheric gravity waves, often also called internal waves, exist in layered atmospheres. They either occur as quasi-periodic waves, solitary waves or undular bores. They are often generated behind mountain ranges in which case they are called lee waves. In the steady state lee waves are stationary with respect to the terrain feature, but they are propagating relative to the mean air flow above the earth surface. Lee waves are very common in visible remote sensing imagery where they manifest themselves as wave-like cloud patterns.

However, they also can manifest themselves on the sea surface since they are associated with varying wind speed at the sea surface and thus a varying short-scale sea surface roughness.
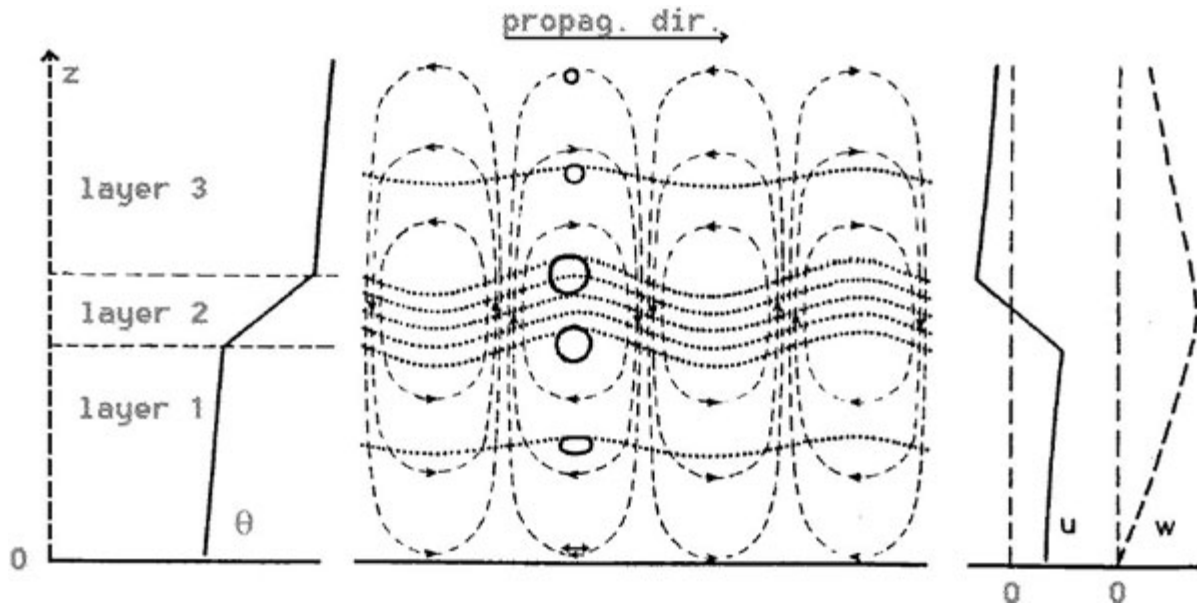

Fig. 1: *A linear gravity wave propagating from left to right in a three-layer atmosphere. (left) Assumed height profile of potential temperature for a stably stratified three-layer atmosphere. (middle) isolines of potential temperature (dotted lines), streamlines (dashed lines), and direction of the wind velocity fluctuations at the sea surface (arrows at the bottom). (right) Amplitudes of the wind speed fluctuations in the direction of the wave propagation and in the vertical direction as a function of height. (Reproduced from Alpers and Stilke, 1996)*
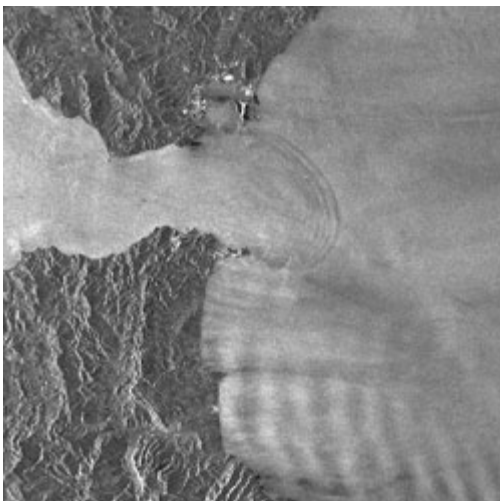

Mediterranean Sea

Latitude: 35° 52' N - Longitude: 05° 14' W

This image shows in the upper part sea surface manifestations of an oceanic internal wave packet generated in the Strait of Gibraltar by the interaction of the tidal flow with underwater bottom features and in the lower part sea surface manifestations of atmospheric lee waves generated by an eastward wind blowing with 7m/s over the 600 m high mountain range Sierra del Hauz in Morocco.

Strait of Gibraltar Sep. 3, 1993, 2239 UT
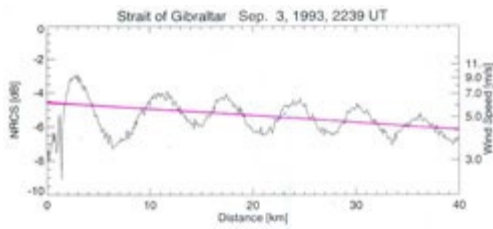
An image intensity scan from west to east through the internal lee wave pattern east of the Maroccan coast is shown in the figure above. On the left-hand vertical coordinate axis the normalized radar cross section (NRCS) is plotted and on the right-hand vertical coordinate axis the wind speed at a height of 10 m above sea level as calculated from the wind scatterometer model CMOD4 (see section "introduction" to "atmospheric phenomena").
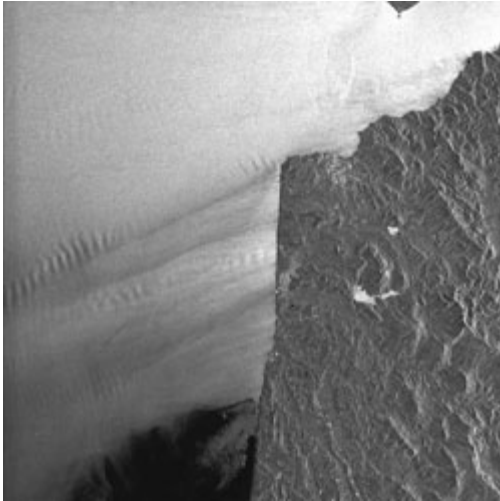
Strait of Gibraltar

Latitude: 35° 38' N - Longitude: 06° 02' W

Gravity waves generated by a easterly wind blowing through the Strait of Gibraltar and over northern Morocco.
The wave train to the north is generated by a horizontal shear in the wind field and the other wave trains are typically lee waves generated by the interaction of the wind with topographic features at Moroccan Atlantic coast.
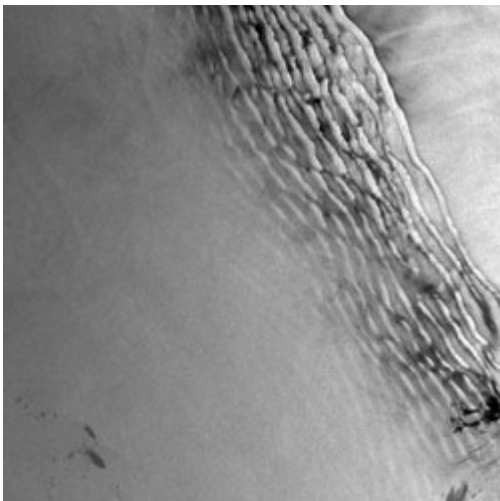
Caspian Sea

Latitude: 40° 57' N - Longitude: 50° 42' E

The wavelike pattern visible in the central part of the Caspian Sea is very likely a sea surface manifestation of a nonlinear atmospheric internal wave packet or of an atmospheric undular bore. Usually such nonlinear wave disturbances in the marine boundary layer are generated by the intrusion of colder, denser air into a stable atmosphere. The modulation structure of this sea surface pattern very strongly resembles a modulation signature detected on an ERS-1 SAR image of the North Sea. By comparison with in-situ data, the latter was identified unambiguously as being caused by a nonlinear wave pertubation in the marine boundary layer. Such wavelike disturbances in the atmosphere are frequently observed phenomena (Vachon et al. (1995), Alpers and Stilke (1996)). The dark patches in the lower part of the image are due to oil pollution.
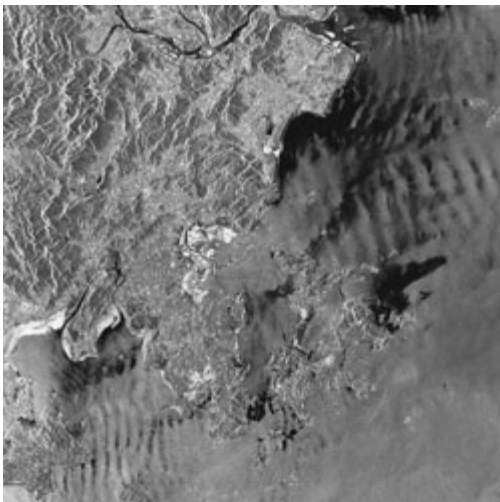
Taiwan Strait

Latitude: 25° 12' N - Longitude: 119° 43' E

Atmospheric lee waves generated by a wind blowing over the mountainous area south of Fuzhou (Fukien, China). The crests of the lee waves are oriented nearly parallel to the coastal mountain ridges.

#	Orbit	Frame(s)	Satellite	Date	Time	Location
1	11168	0711	ERS-1	03-Sep-1993	22:39	
2	25499	2889	ERS-2	06-Jun-2000	11:05	
3	25230	2781	ERS-1	12-May-1996	07:23	
4	17773	0423-0441	ERS-1	08-Dec-1994	14:25	

References

- Alpers, W. & Stilke, G., Observation of nonlinear wave disturbance in the marine atmosphere by the synthetic aperture radar aboard the ERS 1 satellite. J. Geophys. Res., 101, No. C3, 6513-6525 (1996).
- Christie, D.R., Long nonlinear waves in the lower atmosphere, J. Atmos. Sci., 46, 1462-1491 (1989).
- Clark, T.L., Hauf, T. & Kuettner, J.P., Convectively forced internal gravity waves: Results from two-dimensional numerical experiments, Quarterly Journal of the Royal Meteorology Society, 112, 899-926 (1986).
- Crook, N.A., Trapping of low-level internal gravity waves, J. Atmos. Sci., 45, 1533-1541 (1988).
- Drake, V.A., Solitary wave disturbances of the nocturnal boundary layer revealed by radar observations of migrating insects, Boundary Layer Meteorol., 31, 269-286 (1985).
- Fritz, S., The significance of mountain lee waves as seen from satellite pictures, J. of Applied Meteorol., 4, 31-37 (1965).
- Gossard, E.E., Richer, J.H. & Atlas, D., Internal waves in the atmosphere from high-resolution radar measurements, J. Geophys. Res., 75, 3523-3536 (1970).

Menhofer A., Smith, R.K., Reeder, M.J. & Christie, D.R., "Morning-glory" disturbances and the environment in which they propagate. J. Atm. Sci., 54, N 7, 1712-1725 (1997).

- Mitnik, L.M., Hsu, M.-K. & Liu, C.-T., ERS-1 SAR observations of dynamic features in the southern East-China Sea. La mer, 34, 215-225 (1996).
- Rogers, D.P., Johnson, D.W. & Friehe, C.A., The stable internal boundary layer over a coastal sea. Part II: Gravity waves and momentum balance, J. Atmos. Sci., 52, 684-696 (1995).
- Scherhag, R., The Berlin fog waves of Oct. 1969, Berlin Weather Map, Supplement, 155/69, Free University of Berlin, Germany (1969).
- Scorer, R.S., Theory of waves in the lee of mountains, Quarterly Journal of the Royal Meteorology Society, 75, 41-56 (1949).
- Seitter, K.L. & Muench, H.S., Observation of a cold front with rope cloud, Mon. Weather Rev., 113, 840-848 (1985).
- Smith, R.K., Travelling waves and bores in the lower atmosphere: The "Morning Glory" and related phenomena, Earth Sci. Rev., 25, 267-290 (1988).
- Thomson, R.E., Vachon, P.W. & Borstad, G.A., Airborne synthetic aperture radar imagery of atmospheric gravity waves, J. Geophys. Res., 97, 14249-14257 (1992).
- Vachon, P.W., Johannessen, J.J. & Browne, D.P., ERS-1 SAR images of atmospheric gravity waves. IEEE Trans. Geosci. Remote Sensing, 33, 4, 1014-1025 (1995).
- Vachon, P.W., Johannessen, O.M. & Johannessen, J.J., An ERS 1 synthetic aperture radar image of atmospheric lee waves. J. Geophys. Res., 99, No. C11, 22483-22490 (1994).
- Zheng, Q., Yan, X.-H., Klemas, V., Ho, C.R., Kuo, N.-J. & Wang, Z., Coastal lee waves on ERS-1 SAR images. J. Geophys. Res., 103, No. C4, 7979-7993 (1998).

Atmospheric Convective Cells

Introduction

Atmospheric convective cells over the ocean can be formed when a negative air-sea temperature difference gives rise to an unstable stratification of the marine atmospheric boundary layer and thus to a pronounced energy exchange in vertical direction (Agee, 1982, 1984, 1987; Mitnik, 1992; Atkinson and Zhang, 1996). The air is heated from below and warm air bubbles move upwards giving rise to cellular structures (see Fig. 1). Typical convective cells are characterized by a cylindrical flow pattern which is superimposed upon the ambient wind field. The direction of the cellular air flow directly above the sea surface is either radially outward from the center of the cells ("open cells") or from the rim toward the centre ("closed cells"). Open-cell circulation has downward motion and clear sky in the center, and is surrounded by cloud associated with upward motion (Atkinson and Zhang, 1996). Open-cell mesoscale cellular convection is more frequently observed than close-cell mesoscale convection (Busack et al., 1985). Both types of mesoscale convective cells become visible on SAR images because they are associated with a variable wind velocity at the sea surface which modulates the sea surface roughness and thus the NRCS (Mitnik, 1992; Ufermann and Romeiser, 1999).

Usually mesoscale atmospheric convective cells are defined as organised cellular structures in the planetary boundary layer which have cell diameters ranging from 10 to 40 km (Atkinson and Zhang, 1996). However, on ERS SAR images often kilometre-scale backscatter patterns ("mottles") are visible which are attributed to "convective boundary-spinning eddies" (Sikora et al., 1995). According to Kaimal et al. (1976) the horizontal wavelength of the convective boundary-spinning eddies should be a factor of 1.5 larger than the height of the boundary layer. In an investigation carried out by Sikora et al. (1995) over the northwestern edge of the Gulf Stream North Wall the averaged measured wavelength of a mottle was determined to be 1.33 km with a standard deviation of 0.5 km. The aspect ratio (the ratio between the wavelength of the mottled pattern and the boundary layer height) was determined to be 1.98 plus or minus 0.5. This result suggests that it is possible to estimate the height of the marine boundary layer from the characteristic length scale of the kilometre-scale backscatter patterns, associated with convective boundary-spinning eddies.
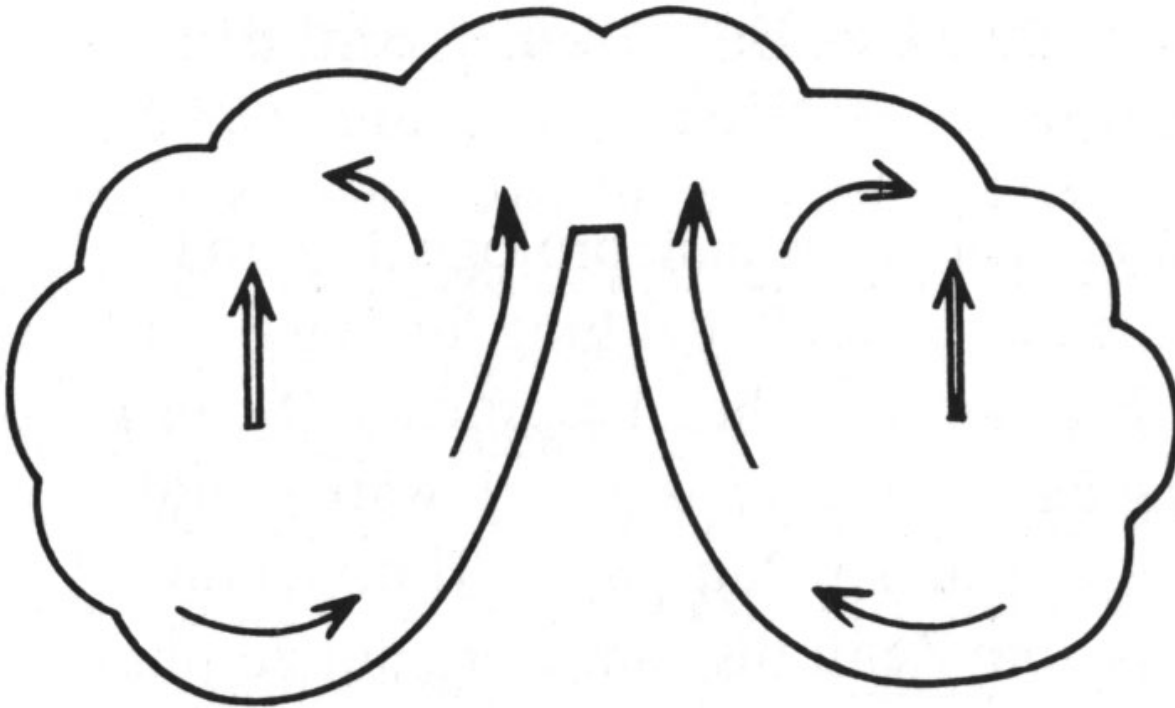

Fig. 1: *Schematic diagram illustrating the convective process where warm air bubbles ascend through the colder atmosphere. The uplifting is caused by heating from below and by mixing with the surrounding colder air (adapted from Liljequist and Cehak, 1979).*

Tyrrhenian Sea

Latitude: 38° 26' N - Longitude: 15° 30' E

The cellular features visible in most parts of this image are sea surface manifestations of such convective cells. On this day the water was 9 °C warmer than the air and thus giving rise to an unstable sea-air interface. The quasi-regular features are absent in a coastal sector adjacent to the northern Sicilian coast. There the convective cells are destroyed by the katabatic wind blowing from the northern Sicilian mountains through the valleys onto the sea.
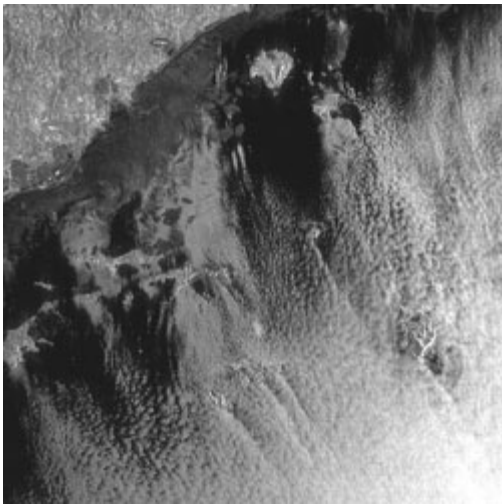
Korea Bay

Latitude: 39° 15' N - Longitude: 122° 48' E

A cold wind is blowing in January from the mountainous Liaodong Peninsula, North East China, over the warm water of the Korea Bay and generates convective cells which have diameters of the order of a few kilometres. Behind the small islands to the south, the cellular structures are disturbed by island wakes.
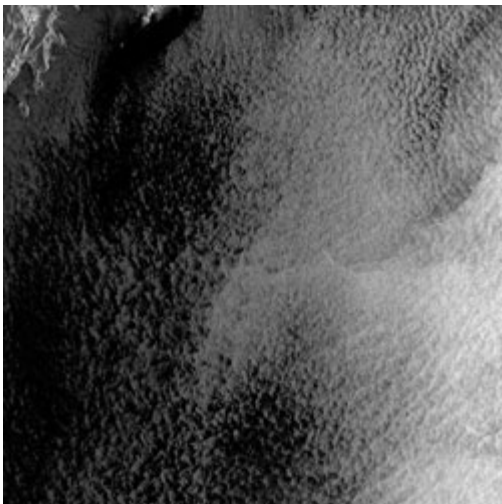
Sea of Japan

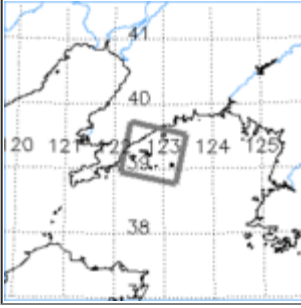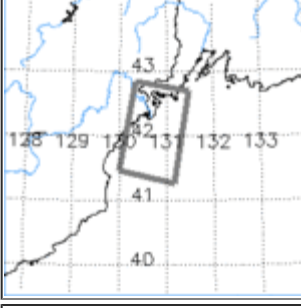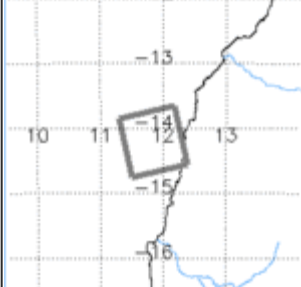Latitude: 41° 49' N - Longitude: 130° 44' E
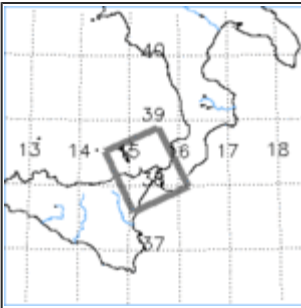
Convective cells generated by a cold northeasterly wind blowing from the mountains of Sikhote-Alin northeast of Vladivostok (Russia) over the Sea of Japan. The river visible in the left-hand section of the image is the border between Russia and Korea.
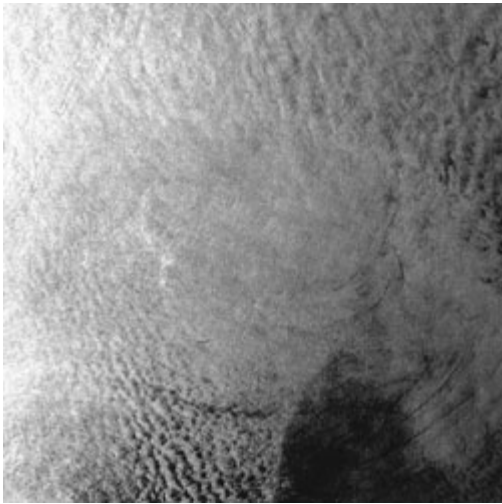
Coast of Angola

Latitude: 14° 12' S - Longitude: 11° 51' E

Convective cells over the Atlantic Ocean near the coast of Angola. The dark area at the bottom of the image is very likely caused by upwelling. Here the water is cooler than west giving rise to a stable air-sea interface.

#	Orbit	Frame(s)	Satellite	Date	Time	Location
1	6104	765	ERS-1	08-Sep-1992	21:13	
2	07935	2817	ERS-1	21-Jan-1993	02:33	
3	20455	2763	ERS-2	20-Mar-1999	02:03	
4	10704	6903	ERS-2	07-May-1997	22:02	

References

- Agee, E.M., An introduction to shallow convective systems, in Cloud Dynamics, edited by E.M. Agee, and T. Asai, 3-30, D. Reidel, Norwell, Mass. (1982).
- Agee, E.M., Observations from space and thermal convection, Bull. Am. Meteorol. Soc., 65, 938-949 (1984).
- Agee, E.M., Meso-scale cellular convection over the oceans, Dyn. Atmos. Ocean., 10, 317-341 (1987).
- Atkinson, B.W. & Zhang, J.W., Mesoscale shallow convection in the atmosphere, Reviews of Geophysics, 34, 403-431 (1996).
- Bakan, S. & Schwarz, E., Cellular convection over the northeastern Atlantic, Int. J. Climatol., 12, 353-367 (1992).
- Boppe, R.S. & Neu, W.L., Quasi-coherent structures in the marine atmospheric surface layer, J. Geophys. Res., 100, 20635-20648 (1995).
- Busack, B., Bakan, S. & Luthardt, H., Surface conditions during meso-scale cellular convection, Contrib. Atmos. Phys., 58, 4-10 (1985).
- Liljequist, G.H. & Cehak, K., Allgemeine Meteorologie, Friedr. Vieweg & Sohn, Braunschweig/Wiesbaden (1979).
- Mitnik, L.M., Mesoscale coherent structures in the surface wind field during cold air outbreaks over the far eastern seas from the satellite side looking radar, Mer., 30, 297-314 (1992).
- Savtchenko, A., Effect of large eddies on atmospheric surface layer turbulence and the underlying wave field, J. Geophys. Res., 104, 3149-3157 (1999).
- Sikora, T.D., Young, G.S., Beal, R.C. & Edson, J.B., Use of spaceborne synthetic aperture radar imagery of the sea surface in detecting the presence and structure of the convective marine atmospheric boundary layer, Monthly Weather Rev., 123, 3623-3632 (1995).
- Ufermann, S. & Romeiser, R., Numerical study on signatures of atmospheric convective cells in radar images of the ocean, J. Geophys. Res., 104, 25707-25719 (1999).
- Young, G.S. & Sikora, T.D., Distinguishing boundary layer signatures from mesoscale, IGARSS'98.

# Atmospheric Boundary Layer Rolls

Introduction

Atmospheric boundary layer rolls are helical circulation patterns in the atmospheric boundary layer which are superimposed on the mean wind field, i.e., the primary flow (see figure below). They can be generated either by thermal instability (Rayleigh-Bénard instability) when the layer is heated from below or cooled from above, or by dynamic instability (inflection point stability) when the wind velocity changes with the height in such a way that an inflection point occurs in the wind component normal to the roll axis. The axes of the boundary layer rolls are oriented between the directions of the mean surface wind and the geostrophic wind above the boundary layer. Usually the boundary layer is capped by an inversion so that the depth of the boundary layer and the roll layer coincide. In the case of a thermal instability, the aspect ratio, i.e., the horizontal wavelength of the roll pattern, l, divided by the roll height, h, is 2.8 according to the linear Rayleigh-Bénard convection. The most frequently observed values range between 2 and 6, but values of up to 15 have been observed [Miura, 1986].

If the moisture conditions are favorable, cloud streets may be formed in the upward rising branches of the roll circulation. Atmospheric boundary layer rolls contribute significantly to the vertical exchange of momentum, heat, and moisture in the atmosphere. At higher altitudes their relative contribution to the total vertical fluxes in the atmosphere can even be larger than the turbulent fluxes. [Alpers et al., 1995].
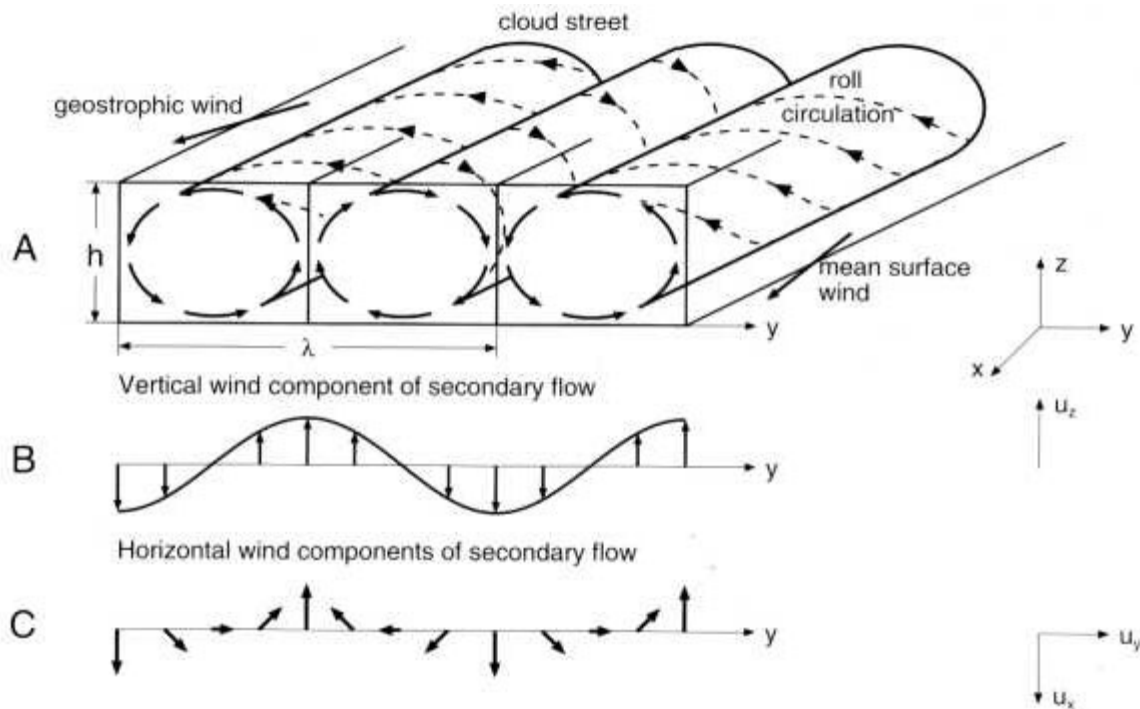

Schematic plot of secondary flow pattern associated with atmospheric boundary layer rolls. Panel A: Perspective view of the three-dimensional flow; Panel B: Variation of the vertical component uz of the wind velocity along the y direction; Panel C: Variation of the horizontal components ux and uy (in the x-y plane).

Ancillary information
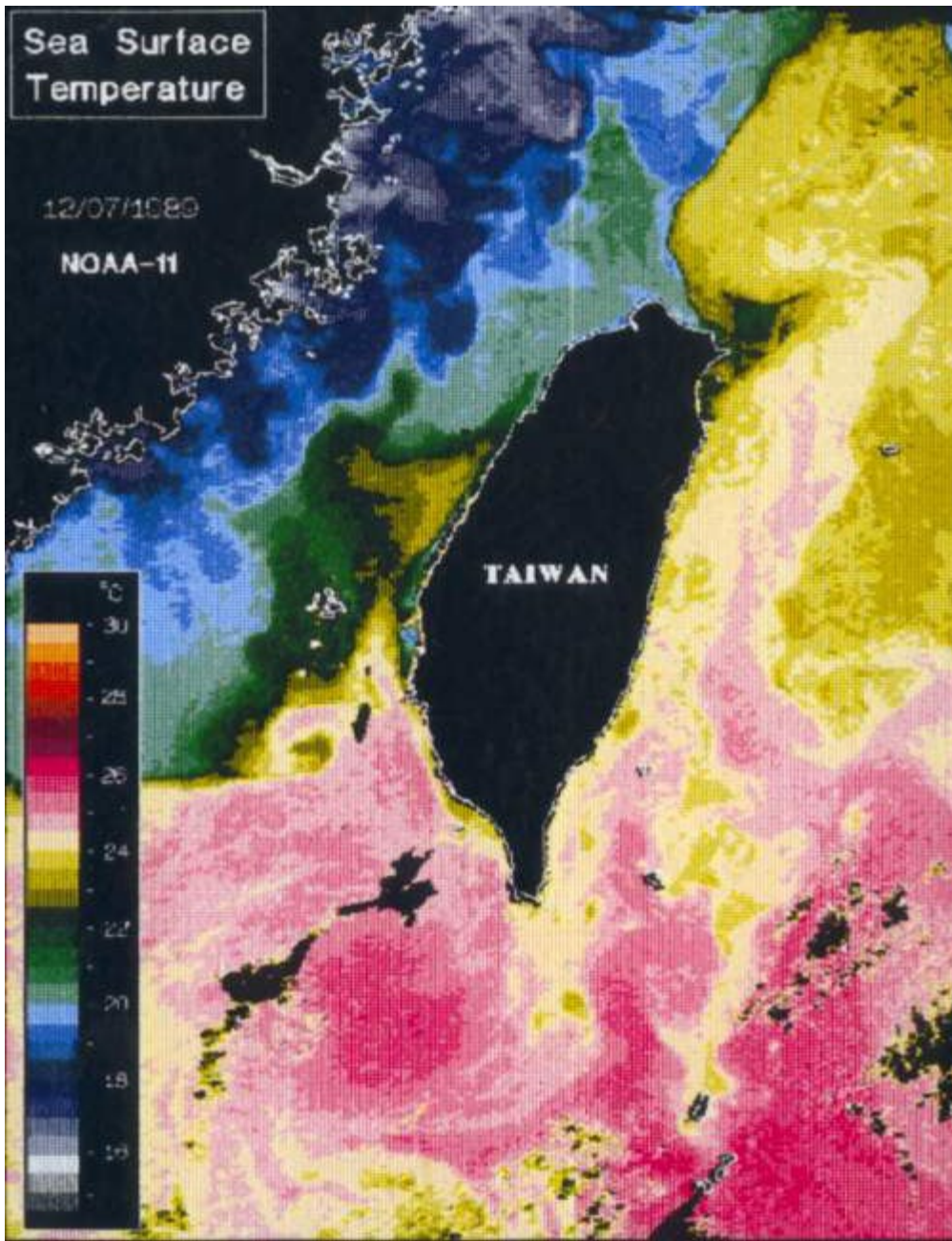
Temperature map derived from NOAA-11 AVHRR data of 7 Dec. 1989, showing that in winter a band of cold water is stretching along the east coast of China. Further to the east the water is warmer.
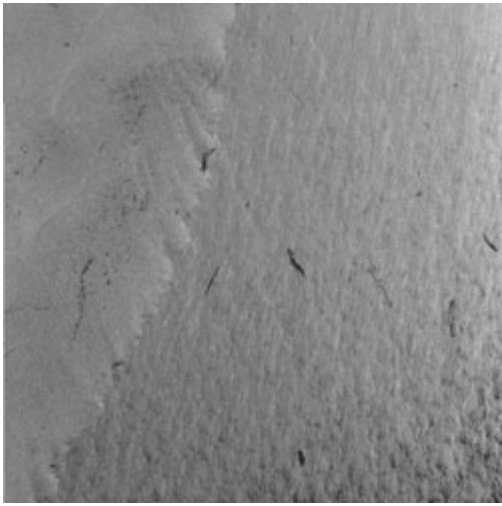
East China Sea

Latitude: 28° 01' N - Longitude: 122° 29' E

Boundary layer rolls in the Taiwan Strait. The line which divides the image into two sections of different textures represents the boundary between water masses of different temperatures. In winter a cold water mass stretches along the east coast of China as is evident also from the AVHRR infrared image of 7 Dec. 1989 shown above. Over the warm water, cold wind blowing from the north generates atmospheric boundary layer rolls, because here the air is heated from below which gives rise to an unstable air-sea interface. The streaky texture of the right-hand section of the image results from imprints of these atmospheric boundary layer rolls on the sea surface. Over the cold water no boundary layer rolls are generated. Note also the numerous black patches in the image which are due to mineral oil spills in this sea area with heavy ship traffic.

Orbit	Frame(s)	Satellite	Date	Time	Location
18196	3033-3051	ERS-1	07-Jan-1995	02:26	

References

- Alpers, W. & Brümmer, B., Atmospheric bondary layer rolls observed by the synthetic aperture radar aboard the ERS-1 satellite, J. Geophys. Res., 99, 12613-12621 (1994).
- Brown, R.A., Longitudinal instabilities and secondary flows in the planetary boundary layer: A review, Rev. Geophys. Space Phys., 18, 683-697 (1980).
- Etling, D. & Brown, R.A., Roll vortices in the planetary boundary layer: A review, Boundary Layer Meteorol., 65, 215-248 (1993).
- Ford, J.P., Cimino, J.B., Elachi, C., Space shuttle Columbia views the world with imaging radar:The SIR-A experiment. Jet Propul. Lab.,Calif. Inst.of Technol., Pasadena, Pul. 82-95 (1983).
- Fu, L.L. & Holt, B., SEASAT views oceans and sea ice with synthetic aperture radar. Jet Prop. Lab., Clif. Int. of Technol., Pasadena, Pul. 81-120 (1981).
- Küttner, J.P., Cloud bands in the atmosphere, Tellus, 23, 404-425 (1971).
- Mitnik,L.M., Mesoscale coherent structures in the surface wind field during cold air outbreaks over the Far Eastern seas from the satellite side looking radar, Extrait de la mer (Bulletin de la Société franco-japanaise d'océ:anographie), Tome 30 (3):287-296 (1982).
- Miura, Y., Aspect ratios of longitudinal rolls and convection cells observed during cold air outbreaks, J. Atmos. Sci., 43, 26-39 (1986).
- Mourad, P.D. & Walter, B.A., Viewing a cold air outbreal using satellite-based synthetic aperture radar and Advanced Very High Resolution Radiometer imagery, J. Geophys. Res., 101, 16391-16400 (1996).
- Müller, G., Brümmer, B. & Alpers, W., Roll convection within an Arctic cold air outbreak: Interpretation of in situ aircraft measurements and spaceborne SAR imagery by a three-dimensional atmospheric model, Mon. Weather Rev., 127, 363-380 (1999).
- Raasch, S., Numerical simulation of the development of convective boundary layer during a cold air outbreak,

Boundary Layer Meteorol., 52, 349-357 (1990).

- Thompson, T.W., Liu, W.T., Weissman, D.E., Synthetic aperture radar observations of the ocean roughness from rolls in an unstable marine boundary layer, J.Geophys.Res., 10,172-175 (1983).
- Weckwerth, T.M., Horst, T.W. & Wilson, J.W., An observational study of the evolution of horizontal convective rolls, Mon. Weather Rev., 127, 2160-2179 (1999).

Katabatic Winds

Introduction

Katabatic winds are cold winds blowing in the evening and night down a sloping terrain ("gravity flow") and, at a coast, over the adjacent sea surface. These winds are generated because during the evening and night, air near the surface cools faster over the land than over the sea. Over mountain slopes a horizontal density difference develops between the cooler air at the slope surface and the free air in the same altitude over the lower ground or sea. This results in a down-hill flow of the cold air. Sea surface manifestations of katabatic wind fields have often been identified on ERS-1 SAR images acquired during the summer over coastal regions adjacent to mountainous areas.

Strait of Messina

Latitude: 38° 26' N - Longitude: 15° 30' E

ERS-1 SAR image showing north-west of the Strait of Messina a bright mushroom like feature generated by a katabatic wind field which extends from the Calabrian coast near the Italian town Gioia into the Tyrrhenian Sea. Furthermore, between the island of Stromboli (upper left hand section of the image) and the Sicilian coast, mottled patterns can be delineated which are sea surface "imprints" of atmospheric convective cells. During the time of the data acquisition the air temperature was 16° and the water temperature 25°. Thus the water is heated from below and convective atmospheric cells are formed. This cellular structure is destroyed in the vicinity of the Sicilian coast by the katabatic wind blowing from the mountains onto the sea. In the lower section of the image an oceanic internal wave train can be seen propagating southwards in the Strait of Messina.

Strait of Messina

Latitude: 39° 26' N - Longitude: 15° 34' E
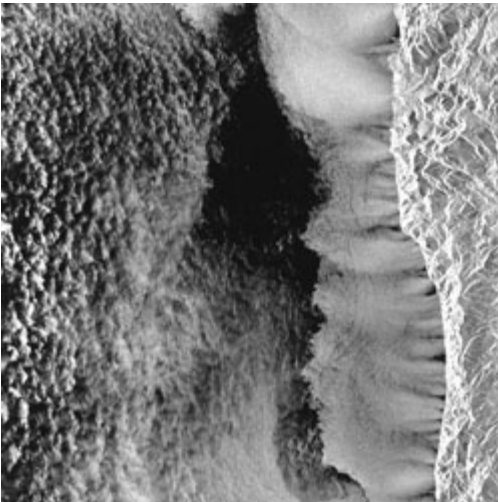
Roughness pattern that stretches like a band along the western coast of Calabria (Southern Italy) and extending seawards for a distance of up to 28 km. Close to the shoreline, the pattern is strongly influenced by orographic features. Coastal valleys can be identified by the associated tongue-like bright patterns on the sea surface. The wind speed and direction measured at Lamezia Terme (located approximately 10 km south of the imaged area) were 2.1 m/s and 270°, respectively. The air temperature was 9.8°C and the water temperature 14.5°. The mottled structure in the left section of the image is the sea surface manifestation of convective cells.
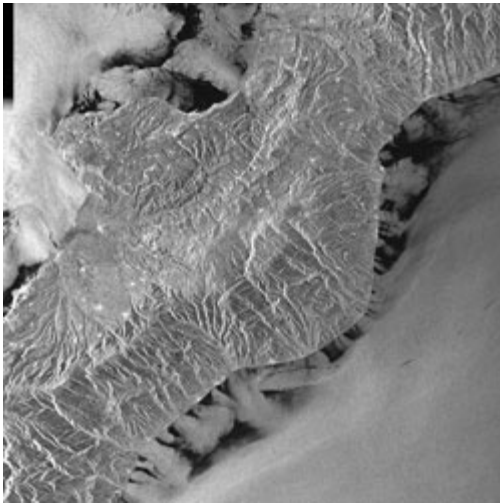
Calabria

Latitude: 38° 30' N - Longitude: 16° 21' E

In the right-hand section of this image katabatic wind fields are visible at the eastern coast of Calabria. The roughness patterns closely mirror the coastal valleys.
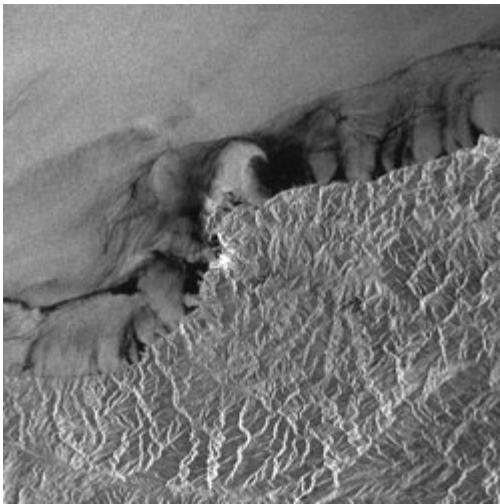
Black Sea

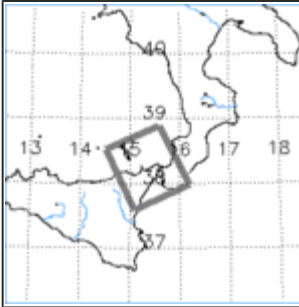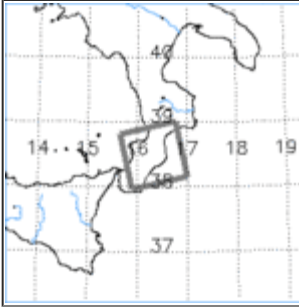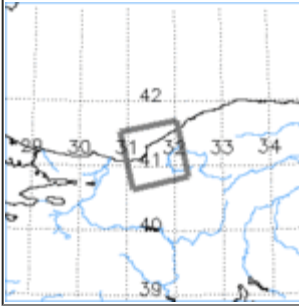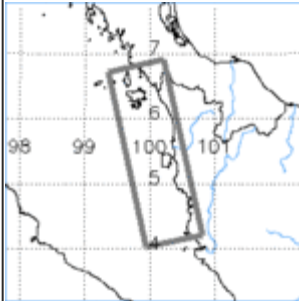Latitude: 41° 11' N - Longitude: 31° 35' E

Katabatic wind fields at the Turkish coast of the Black Sea.

Andaman Sea

Latitude: 05° 29' N - Longitude: 100° 05' E

ERS-1 SAR strip acquired over the Andaman Sea at the west coast of Malaysia and Thailand. The bright band starting slightly north of the Malaysian island of Pinang and extending southward along the coast line has its correspondence in a mountain range located approximately 20 km inland, which extends over this distance from north to south. The SAR data were acquired approximately at local midnight. Thus the bright band can only be caused by katabatic winds originating at this mountain range.

#	Orbit	Frame(s)	Satellite	Date	Time	Location
1	6014	765	ERS-1	08-Sep-1992	21:13	
2	18839	0783	ERS-1	20-Feb-1995	21:13	
3	9249	0765	ERS-1	22-Apr-1993	21:10	
4	15882	0819	ERS-1	29-Jul-1994	20:08	
5	25350	0081-0099-0117	ERS-1	20-May-1996	15:57	

References

- Alpers,W , Measurement of mesoscale oceanic and atmospheric phenomena by ERS-1 SAR, Radio Science Bull., 1995, 275,14-275,22.
- Alpers, W., Pahl, U. & Gross, G., Katabatic wind fields in coastal areas studied by ERS-1 synthetic aperture radar imagery and numerical modeling, J. Geophys. Res., 1998, 103, 7875-7887.

- Gross, G., Numerical simulation of the nocturnal flow systems in the Freiburg area for different topographies, Contrib. Atmos. Phys., 1989, 62, 57-72.
- Gross, G., Anwendungsmöglichkeiten mesoskaliger Simulationsmodelle dargestellt am Beispiel Darmstadt, I, Wind- und Temperaturfelder, Meteorol. Rundsch., 1991, 43, 97-112.
- Gudiksen, P.H., Leone, J.M., King, C.W., Ruffieux, D. & Neff, W.D., Measurements and modeling of the effects of ambient meteorology on nocturnal drainage flows, J. Appl. Meteorol., 1992, 31, 1023-1032.
- McNider, R.T. & Pielke, R.A., Numerical simulation of slope and mountain flows, J. Appl. Meteorol., 1984, 23, 1441-1453.

Land-Sea Breeze

Introduction

Land-sea breeze is caused by the generally different temperatures of the land and the sea, which produce an across-coast air temperature contrast. During the day the wind blows landwards (sea breeze), and during the night it blows seawards (land breeze). Wind speeds associated with land-sea breeze are typically less than 5 m/s and the off-shore flowing air layer is often less than 100 m deep. Land breeze is often contaminated with stronger and deeper terrain-induced katabatic air flows. The intensity of land-sea breeze circulation is strong when the coastal land is dry and only lightly vegetated (Segal et al., 1988). The land-sea breeze system has several effects, among others, (1) it alters the direction and speed of the atmospheric boundary layer winds, (2) it influences the low-level stratiform and cumuliform clouds, (3) it initiates, suppresses and modifies precipitating convective storms, and (4) it recirculates and traps pollutants released into the air.

- West coast of Morocco
- East coast of Taiwan

References

- Defant, F., Theorie der Land- und Seewinde, *Archiv fü̃r Meteorologie, Geophysik, und Bioklimatologie, Vienna*, **Ser. A, 2-3**, 404-425 (1950).
- Haurwitz, B., Comments on the sea-breeze circulation, *J. Meteorol.*, **4**, 1-8 (1947).
- Pielke, R.A., Mesoscale meteorological modeling, *Academic Press, New York*, 612 pp. (1984).
- Rotunno, R., On the linear theory of land and sea breeze, *J. Atmos. Sci.*, **40**, 1999-2009 (1983).
- Segal, M., Avissar, R., McCumber, M.C. & Pielke, R.A., Evaluation of vegetation effects on the generation and modification of mesoscale circulations, *J. Atmos. Sci.*, **45**, 2268-2292 (1988).
- Simpson, J.E., Sea breeze and local winds, *Cambridge Univ. Press*, New York, 234 pp. (1994).
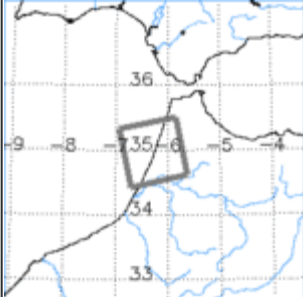
West Coast of Morocco
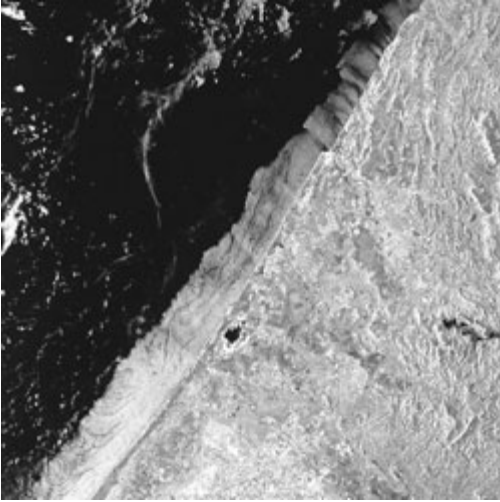
West coast of Morocco

Latitude: 34° 59' N - Longitude: 6° 16' W

Image of the Moroccan Atlantic coast near Larache located at the Makhazen River (upper part of the image). The bright band following the coast line is caused by a wind blowing late in the evening and at night from the land onto the sea. This land breeze is caused by the fact that after sunset the air over land cools off faster than over the sea. The air in the northern mountainous area is funneled through the valleys causing the tongue-like bright patterns on the sea surface.

Orbit	Frame(s)	Satellite	Date	Time	Location
18639	0693	ERS-1	06-Feb-1995	22:44	

East Coast of Taiwan

East coast of Taiwan

Latitude: 23° 30' N - Longitude: 121° 48' E
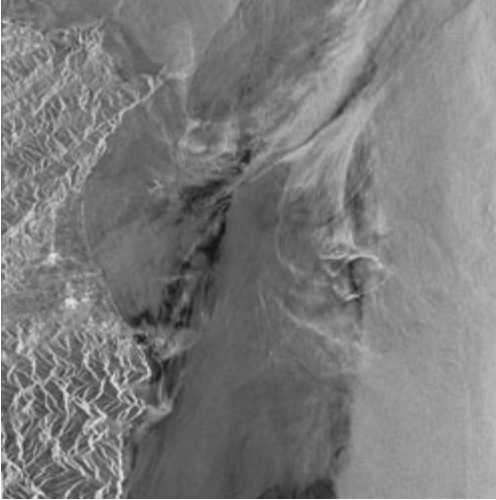
SAR strip of five ERS-1 SAR frames acquired over the coastal waters east of Taiwan on 23 April 1995 at 2:25 UTC, i.e., at 11:25 local time. It shows in the central section adjacent to the coast a low-wind speed area which, to the east, is confined by a frontal line, and it shows in the northern and southern sections features which result from the interaction of the Kuroshio current with shallow underwater topography (in the northern section) and with islands (in the southern section). The low wind speed area (dark area in the image) is an area of descending air and the frontal line is an atmospheric front separating the area of descending air from the ambient wind field. They have their origin in the following meteorological processes: During a cloud-free day the coastal land areas are heated up by solar radiation where the air is lifted up. As a consequence, air has to flow in from the ocean which gives rise to sea breeze and to a atmospheric circulation pattern in which the previously uplifted air over land descends over the ocean. The area of descending air typically extends 20 to 50 km from the coast line. The boundary between the area of descending air and the ambient wind field is a zone of convergence where often clouds (cumulus congestus or cumulus nimbus) and rain cells develop. We attribute the fact that the area of descending air (sea breeze area) appears in some sections of the SAR image dark to low wind speed which is below threshold for ripple wave (Bragg wave) generation (2-3 m/s). According to the weather map the wind was blowing with 3-4 m/s from south.
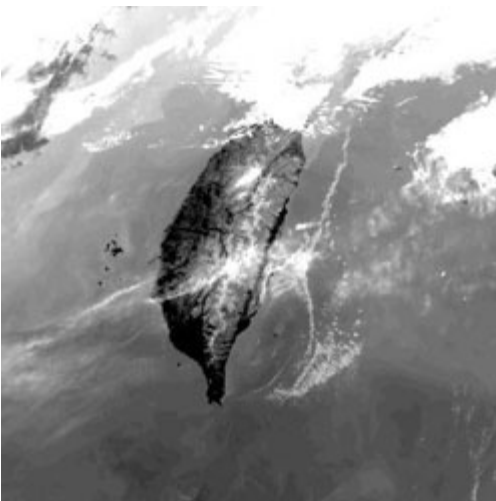
Taiwan

Latitude: 23° 30' N - Longitude: 120° 00' E

NOAA-9 AVHRR infrared image (channel 4) of the waters surrounding Taiwan, which was acquired on 24 April 1994 at 1:13 UTC, i.e., 23 hours and 8 minutes later than the ERS SAR image, but approximately at the same time of the day (1 hour and 12 minutes earlier). The weather conditions on 24 April and 23 April were quite similar. Visible is a cloud band which is located approximately at the same position as the front visible on the ERS-1 SAR image. This is a clear indication that the front visible on the ERS-1 SAR image is of atmospheric origin. Note that the cloud band follows closely the coastline which is a clear indication that it has its origin in an interaction of the atmosphere with the island. On both days the sky was almost cloud-free such that the low-land coastal areas could be heated up by solar radiation. Evidence of this is provided also by this infrared image where dark areas represent warm areas.
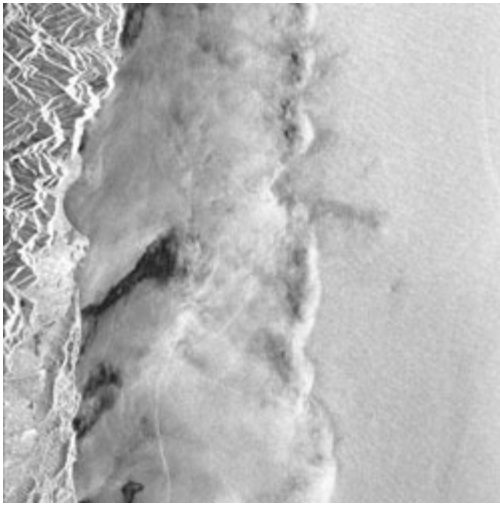
East coast of Taiwan

Latitude: 22° 40' N - Longitude: 121° 39' E

SAR strip of five ERS-2 SAR frames acquired over the coastal waters east of Taiwan on 18 January 1999 at 2:26 UTC, i.e., at 11:26 local time. It shows adjacent to the coast a broad band of distinct texture, which is approximately 50 km wide. We interpret this band as the sea area, where the air associated with the sea breeze circulation descends to the sea surface. Since this image was acquired during winter, the sea surface temperature was probably higher than the air temperature which gives rise to an unstable air-sea interface and thus favours the generation of turbulence. The inhomogeneous texture of the band is very likely caused by turbulence. The atmospheric front separating the area of descending air from the ambient wind field appears as a bright band on the SAR image with interdispersed black patches in the northern section. The bright band results from strong convergence in the frontal zone which gives rise to increased sea surface roughness. We interpret the bright band in the northern section with interdispersed black patches as sea surface manifestation of he atmospheric front in which rain cells are embedded. According to the weather map the wind was blowing with 3-5 m/s from SE. This wind direction is consistent with the direction of the wind streaks visible on the ERS-1 SAR image.

#	Orbit	Frame(s)	Satellite	Date	Time	Location
1	19716	3105-3123-3141-3159	ERS-1	23-APR-1995	02:25	
2	53413	-	NOAA-9	24-Apr-1995	01:33	
3	19582	3105-3123-3141-3159-3177-3195	ERS-2	18-Jan-1999	02:26	

Atmospheric Fronts

Introduction

Atmospheric fronts are boundaries of air masses with different properties. Often atmospheric fronts separate air masses of different temperatures. Usually the wind speed and wind direction are different at both sides of an atmospheric front. Over the ocean this results in a differing short-scale sea surface roughness and thus on the SAR image atmospheric fronts appear as boundaries between areas of different image intensity, which easily can be delineated on SAR images of the sea surface.
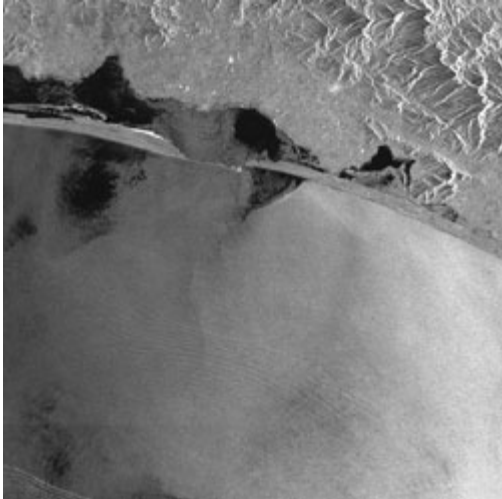
Mexico

Latitude: 15° 30' N - Longitude: 94° 00' W

Visible on this ERS-2 SAR image is a bright area near the coast which results from wind which is blowing from the mountains in the Isthmus of Tehuantepec (Mexico) onto the eastern tropical Pacific Ocean. Also visible are sea surface manifestations of several oceanic internal wave packets. Note that in the area with a higher wind speed the internal waves have a lower image contrast. This is a consequence of the fact that the hydrodynamic modulation of the short surface waves ("Bragg waves") by a variable current decreases with wind speed.
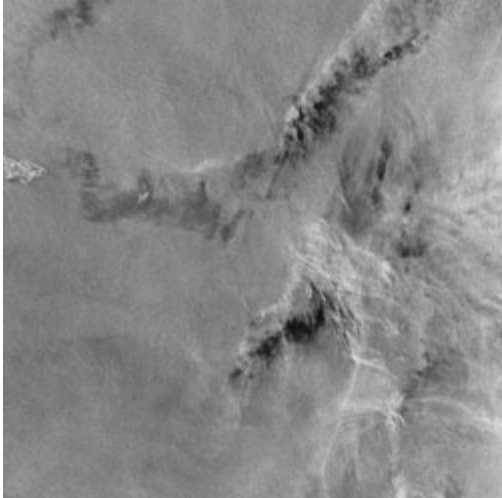
Sakishima-gunto

Latitude: 23° 49' N - Longitude: 122° 42' E

Atmospheric front near Taiwan. The dark and bright bands on the SAR image extending from NE to SW result from an atmospheric front that moves in a southeastward direction. The surface analysis map of the Japan Meteorological Agency of December 14, 1994 at 12 UTC shows an occlusion front located approximately at the position of the bands in the SAR image The bright band is very likely caused by a squall line ahead of the front, while the dark band and the dark patches are caused by rain impinging onto the sea surface where they generate turbulence in the uppermost water layer and thus damp the C band Bragg waves. Behind the front the image intensity is almost uniform indicating a uniform wind field. The wind direction in this backward side of the front can be obtained from the direction of the faintly visible streaks,which are oriented almost normal to the dark band and which are sea surface imprints of atmospheric boundary layer rolls.
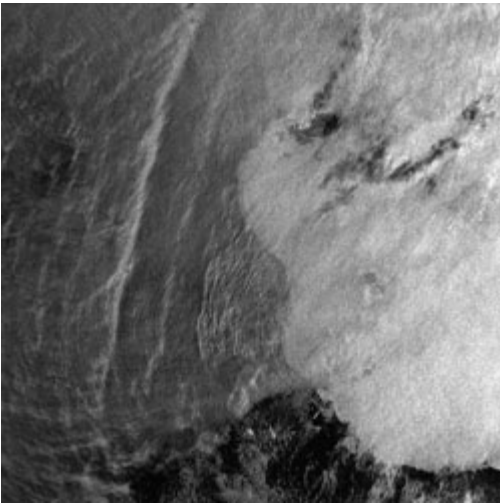
**Sulu Sea**

Latitude: 8° 21' N - Longitude: 118° 32' E

The bright area in the right-hand section of this image is caused by winds (downdrafts) associated with tropical rain cells. Sea surface manifestations of oceanic internal waves are also visible on this image.
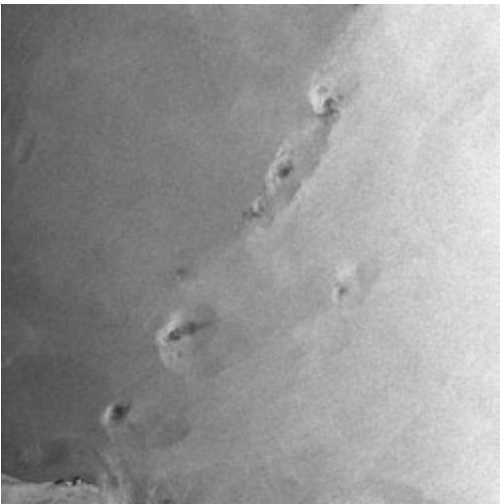
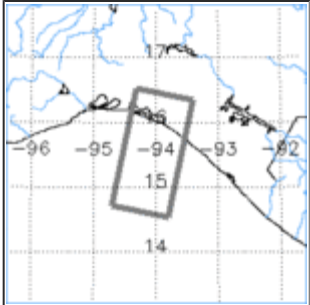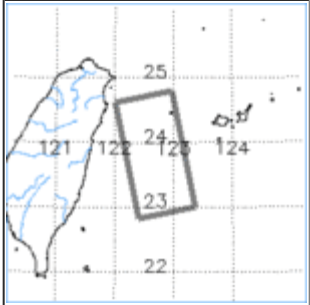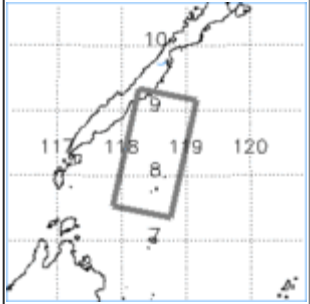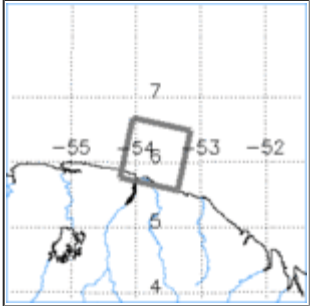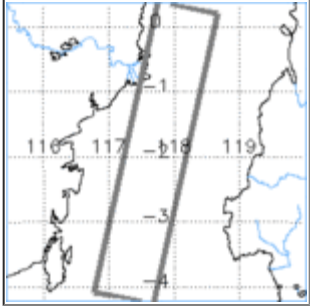**Surinam**

Latitude: 6° 08' N - Longitude: 53° 42' W

This ERS-1 SAR image shows an atmospheric front in the tropical Atlantic with several small tropical rain cells embedded (the irregular patches with dark areas).
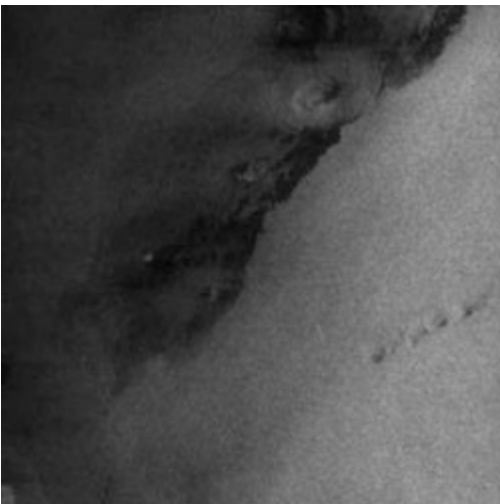
Makassar Strait

Latitude: 1° 56' S - Longitude: 117° 43' E

In the upper part of this image an atmospheric front with several associated rain cells can be delineated. In the lower part the gust front of a large cluster of rain cells is visible.

#	Orbit	Frame(s)	Satellite	Date	Time	Location
1	03444	3285-3303	ERS-2	17-Dec-1995	16:44	
2	17859	0459-0477	ERS-1	14-Dec-1994	14:15	
3	24091	3429-3447	ERS-2	29-Nov-1999	02:29	
4	04220	3483	ERS-1	06-May-1992	13:31	
5	10521	3609-3627-3645-3663-3681	ERS-2	25-Apr-1997	02:27	

Island Wakes

Introduction

When a strong wind blows against a mountainous island, then on SAR images often a wake pattern can be delineated on the leeward side of the island. Sometimes the wake pattern consists only of a streak of reduced sea surface roughness due to wind shadowing, but often it exhibits some regular structure due to atmospheric eddies. However, some of the radar signatures visible on SAR images in the lee of mountainous island may also originate from oceanic phenomena which are wind-induced.
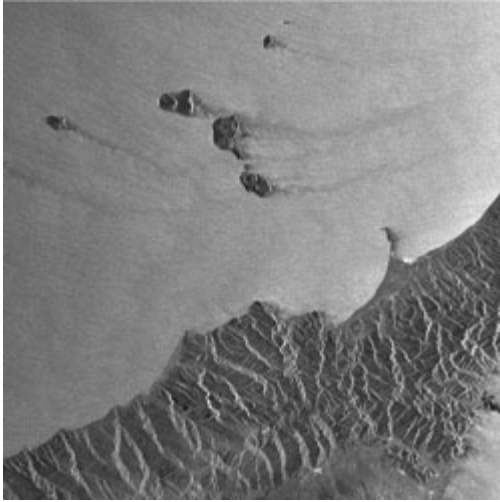
Isole Lipari

Latitude: 38° 16' N - Longitude: 14° 56' E

Wakes behind the Italian islands Filicudi, Salina, Lipari, Vulcano, and Panaria (from west to east) generated by a strong westerly wind. These islands are of volcanic origin and have volcanic cones, whose heights are 773 m, 962 m, 603 m, 499 m, and 420 m, respectively.
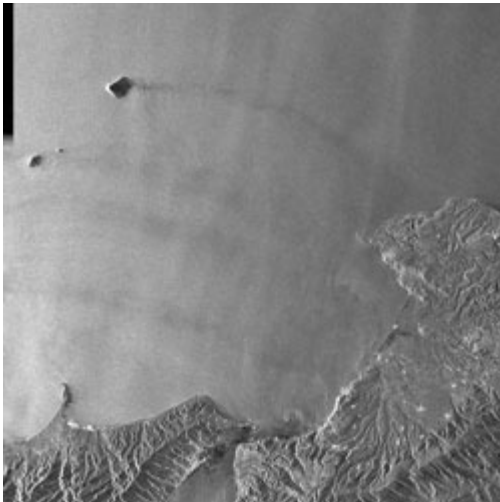
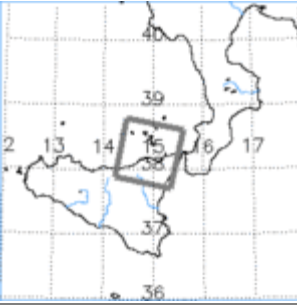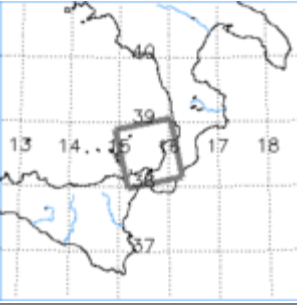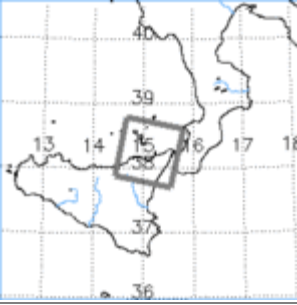**Isole Lipari**

Latitude: 38° 32' N - Longitude: 15° 37' E

Atmospheric wakes behind Isole Lipari in the Tyrrhenian Sea generated by a strong westerly wind. The island in the upper section of the image is the island Stromboli consisting of a volcano which is 926 m high.
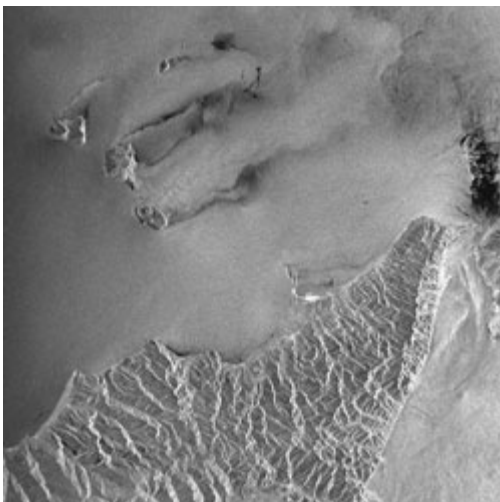
Isole Lipari

Latitude: 38° 16' N - Longitude: 15° 08' E

Gap winds and wakes behind the islands of Lipari (from top to bottom) Panaria, Salina, Lipari, and Vulcano.

| #	Orbit	Frame(s)	Satellite	Date	Time	Location
1	14670	2835	ERS-1	06-May-1994	09:43	
2	09020	0747	ERS-1	06-Apr-1993	21:13	
3	15488	2835	ERS-1	02-Jul-1994	09:41	

References

- Chopra, K.P. & Hubert, L.F., Mesoscale eddies in wake of islands, J. Atm. Sciences 22, 652-657 (1965).
- Mitnik, L.M., Atmospheric and oceanic vortex streets: Observations by satellite radars, In: PORSEC'98.
- Pan, F. & Smith, R.B., Gap winds and wakes: SAR observations and numerical simulations, J. Atm. Sciences 56, 905-923 (1999).
- Smith, R.B. & Grubisic, V., Aerial observations of Hawaii's wake, J. Atm. Sciences 50, 3728-3750 (1993). (A historical note on the death of Captain James Cook).
- Smith, R.B., Gleason, A.C. & Gluholsky, P.A., The wake of St. Vincent, J. Atm. Sciences 54, 606-623 (1997).

Coastal Winds

Near the coast, local winds are often encountered, which can have different origins. Under separate headings we have already mentioned land-sea breeze and katabatic winds. But there exist also other mesoscale coastal winds, e.g., gap winds, that can be detected on SAR images of the sea surface. Some examples are shown in this section.

- Philippines
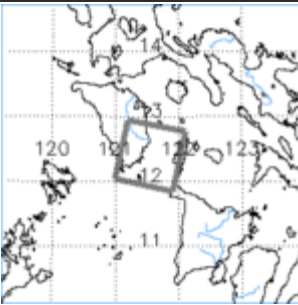- Canary Islands
- Peru
- Taiwan

Coastal Winds - The Philippines
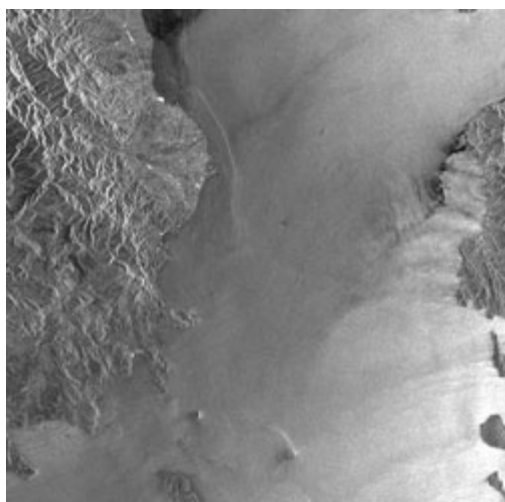
Philippines

Latitude: 12° 25' N - Longitude: 121° 34' E

Gap winds blowing from the east through the Tablas strait separating the Philippine islands Mindoro and Panay. In this strait are located the islands Semivara, Caluya, and Sibay which disturb the wind field.

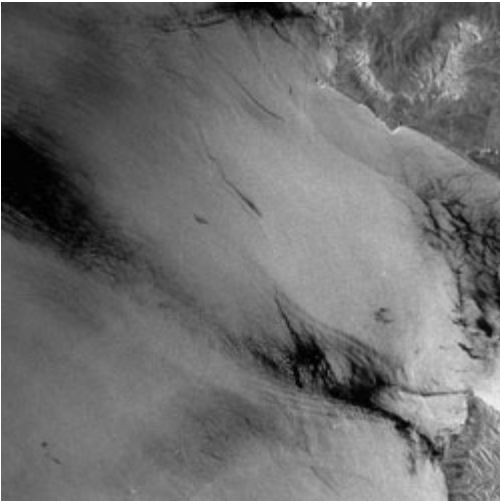| Orbit	Frame(s)	Satellite	Date	Time	Location
04738	3357	ERS-2	17-Mar-1996	02:20	

Coastal Winds - Canary Islands

Canary Islands

Latitude: 28° 30' N - Longitude: 16° 23' W

Local wind blowing around the north eastern tip of the Canarian island Tenerife.

Orbit	Frame(s)	Satellite	Date	Time	Location
19879	3033	ERS-1	04-May-1995	11:42	

Coastal Winds - Peru

Peru

Latitude: 05° 30' S - Longitude: 81° 24' W

Wind blowing from the land over Punta Nermete in Peru (lower right-hand section of the image) forming a very peculiar wake pattern on the sea surface.

Orbit	Frame(s)	Satellite	Date	Time	Location
04221	3717	ERS-1	06-May-1992	15:41	

Coastal Winds - Taiwan
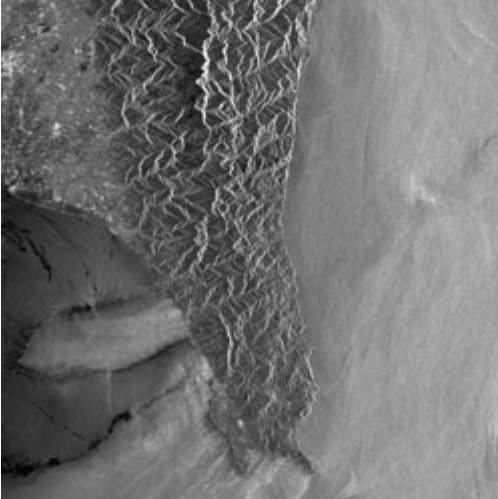
South of Taiwan

Latitude: 22° 18' N - Longitude: 120° 50' E

Coastal winds at the southwest coast of Taiwan. The wind tongue visible in the central left-hand section of the image is very likely induced by strong synoptic-scale winds blowing from the east. The wind is funneled across the island through a gap in the mountains which results in an increase in speed. Note the mountain ridge in the the north-south direction located inland between this wind tongue and the other high wind speed area further south. This ridge is an obstacle to the wind and gives rise to a wind shadow.

Orbit	Frame(s)	Satellite	Date	Time	Location
23996	3159	ERS-1	16-Feb-1996	02:29	

Rain Events

Introduction

Radar signatures of rain in SAR images of the sea surface result from several different physical processes. The most important processes contributing to these radar signatures are: (1) the backscattering of the microwaves at the short surface waves ("Bragg waves") whose amplitudes are modified by rain drops impinging on the sea surface, (2) the roughening of the sea surface by the wind gusts associated with rain cells, and (3) attenuation and scattering of the microwaves by the rain drops in the atmosphere.

Rain Drops impinging on the sea surface generate ring waves which enhance the sea surface roughness [Moore et al., 1979; Bliven et al., 1997; Craeye et al.1997], but they also generate turbulence in the upper water layer which attenuates the short surface waves [Nystuen, 1990; Tsimplis, 1992]. Analyses of multifrequency SIR-C/X-SAR data acquired over tropical and subtropical ocean areas [Melsheimer et al., 1998a] and laboratory measurements at a wind wave tank have shown that the modification of the sea surface roughness by impinging rain drops depends strongly on the wavelength of the water waves: The net effect of the impinging rain drops on the sea surface is a decrease of the amplitude of those water waves which have wavelengths above 10 cm and a decrease of the amplitude of those water waves which have wavelengths below 5 cm. Unfortunately, the critical wavelength at which the increase of the wave amplitude turns into a decrease is not well defined. It depends on the rain rate, the drop size distribution, the wind speed, and the temporal evolution of the rain event. At the initial stage of the rain event, the turbulence in the upper water layer is not fully developed and thus its damping effect on the water waves is small. On the other hand, after it has stopped raining, the turbulence is not decaying immediately (the life time is of the order of a minute) and it keeps damping the waves even after the rain event has ended. The Bragg wavelength over the ERS SAR lies between 8.2 cm and 6.5 cm. Unfortunately, these wavelengths lie in the transition region where, depending on the rain rate, the drop size distribution, the wind speed, and the time history of the rain event, the impinging rain drops can give rise to either an increase or a decrease of the amplitude of the Bragg waves and thus to an increase or a decrease of the NRCS.

In addition to the modification of the sea surface roughness by the impact of rain drops, the sea surface roughness is also affected by the airflow associated with the rain event. Precipitation from a rain cell usually produces a downward airflow (downdraft) by entrainment and by evaporative cooling under the cloud (see, e.g., Cotton and Anthes, 1989). When the downdraft reaches the sea surface, it spreads radially outward as a strong local surface wind which increases the sea surface roughness. This is shown schematically in the figure below. The outer edge of this airflow is called a gust front. If the ambient wind field is weak and does not disturb this airflow pattern, the radially spreading downdraft is visible on SAR images of the sea surface as a nearly circular bright pattern with a sharp edge [Atlas, 1994a; b]. Such a pattern is usually less bright in the center, where the downdraft reaches the ground and horizontal wind speeds are lowest. The lower the ambient wind speed, the higher is the contrast between such a bright pattern and the surroundings. Therefore, radar signatures of rain cells are often more pronounced over tropical oceans where low wind speeds prevail. When a strong ambient wind field is present, then the radially symmetric airflow pattern is distorted and the resulting radar signature is likewise distorted and shows bright as well as dark areas.
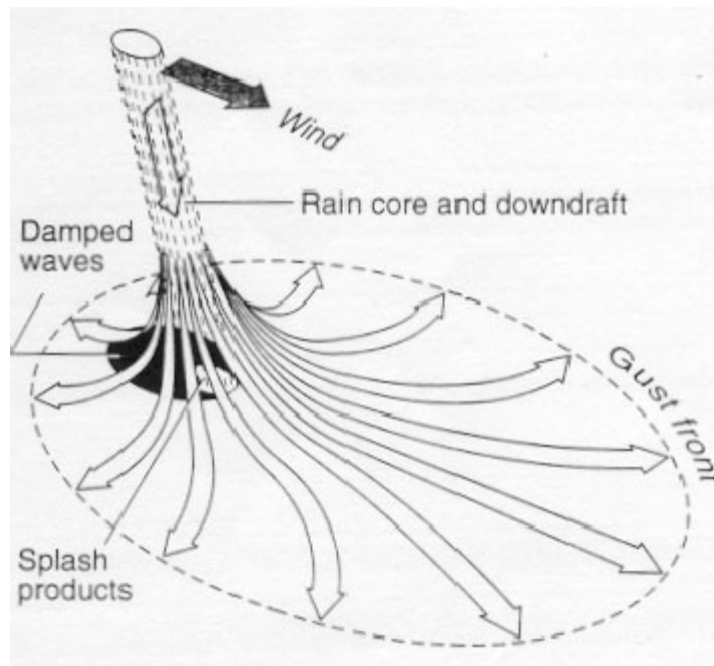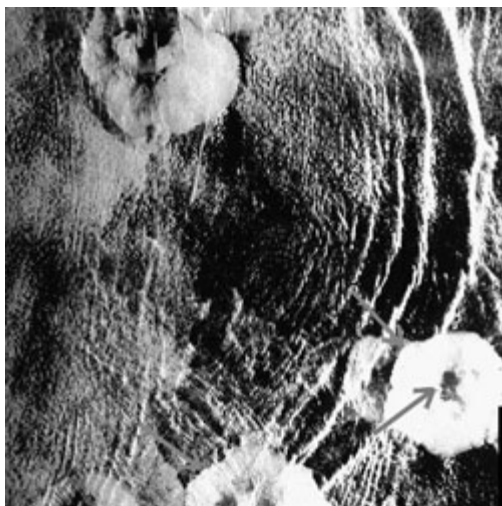
Fig.1: *Schematic sketch of the downdraft of a rain cell, spreading over the sea surface and causing roughening of the sea surface; (adapted from Atlas, 1994b).*

**Andaman Sea**

Latitude: 8° 48' N - Longitude: 94° 56' E

ERS -1 SAR image acquired over the Andaman Sea west of the Nicobar islands during calm wind conditions. The circular bright patterns with a dark hole in the centre are sea surface manifestations of tropical rain cells. The two arrows inserted into the figure point (1) to the gust front of the rain cell and (2) to the area where the Bragg waves are strongly damped by the turbulence generated by rain drops impinging onto the sea surface. Also visible are sea surface manifestations of packets of internal solitary waves.

Gulf of Thailand

Latitude: 9° 46' N - Longitude: 100° 38' E

Cluster of rain cells over the Gulf of Thailand. The inserted arrows point to the gust fronts of the rain cells and to the areas where the Bragg waves are strongly damped by the turbulence generated by heavy rainfall, respectively.
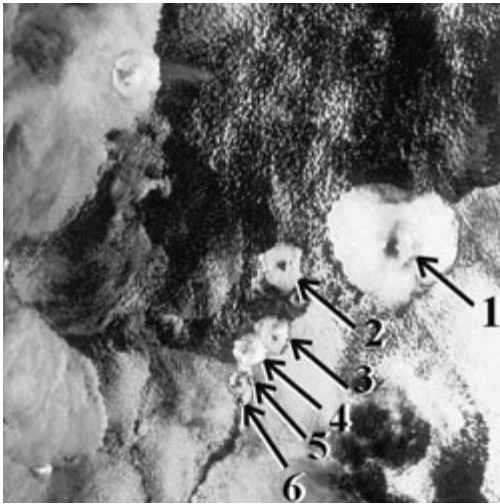
Gulf of Thailand

Latitude: 10° 39' N - Longitude: 100° 49' E

A string of rain cells with decreasing diameters (marked "1" to "6"). The 6 rain cells are very likely at different stages of their life cycles. The more time has elapsed since the downdraft has first reached the sea surface, the larger the diameter of the gust pattern at the sea surface. Thus the rain cell 1 should be the oldest, and the rain cell 6 the youngest cell. (See image below).
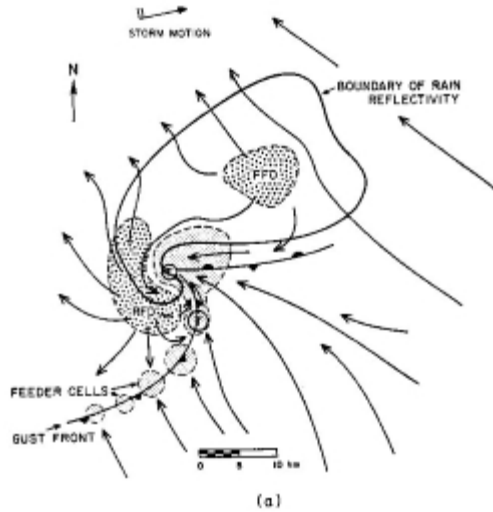
Gulf of Thailand - Plan view of surface weather

Plan view of surface weather, showing locations of the forward-flank and rear-flank downdrafts. The solid line outlines the rainy area usually mapped by radar. Note the hooklike feature. Downdraft and updraft regions are delineated by coarse and fine stippling, respectively. T designates the most likely location where tornados form. [Adapted from Lemom and Doswell (1979), courtesy of R.Davies-Jones.]
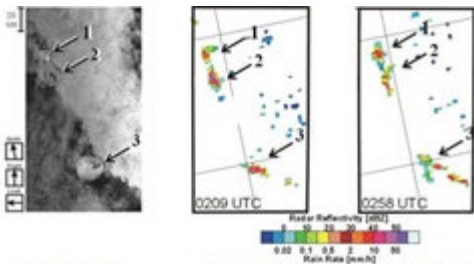
South China Sea

Latitude: 21° 19' N - Longitude: 116° 21' E

Comparison of an ERS-2 SAR image acquired over the South China Sea showing radar signatures of rain cells with two weather radar images acquired 35 minutes before and 12 minutes after the ERS-2 SAR data acquisition. The weather radar is a C-band radar and is located at Dongsha Island (20° 42'N, 116° 44'E), approximately 100 km away from the rain cells. The radar reflectivity measured by the weather radar is converted into rain rate and plotted in the two figures on the right. Comparison of the ERS-2 SAR and the weather radar images clearly show that the circular patterns on the SAR image are caused by rain cells. From the displacement of the radar signatures in the two weather radar images we conclude that the rain cells moved eastward with a speed of about 5 km/h (reproduced from Melsheimer et al., 2000).
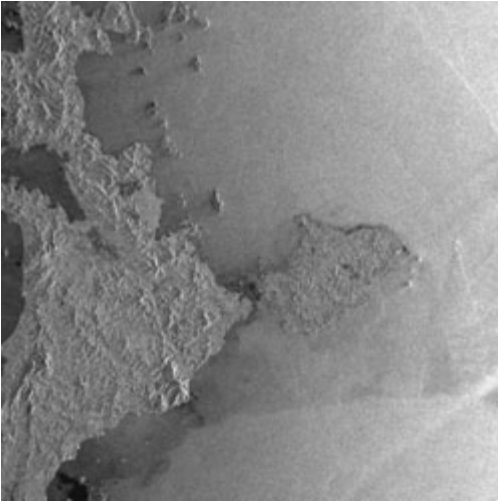
Sulu Sea

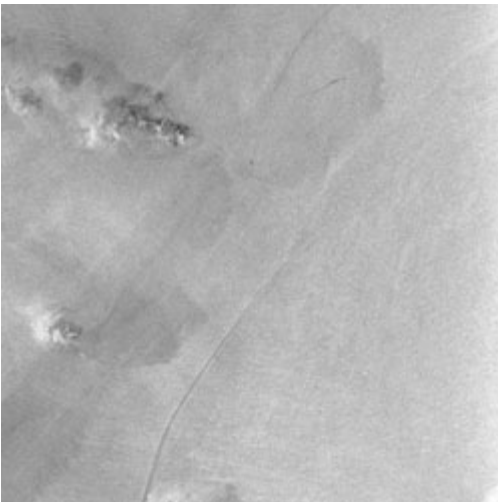Latitude: 10° 08' N - Longitude: 119° 10' E

ERS-2 SAR image acquired over the Sulu Sea near Palawan Island (Philippines). Several small-scale rain cells located at or near an atmospheric front are visible.

Sumatra
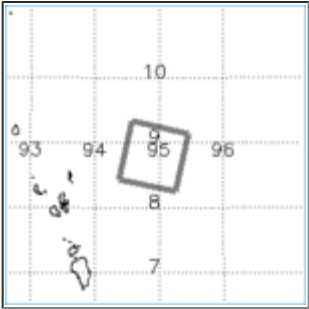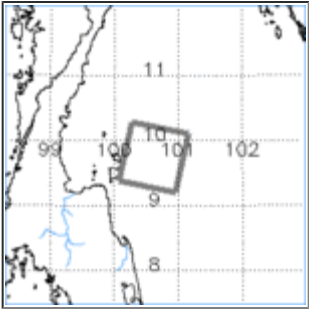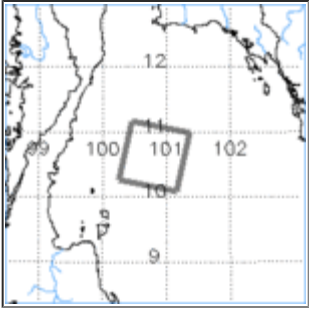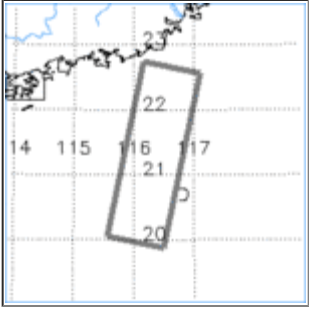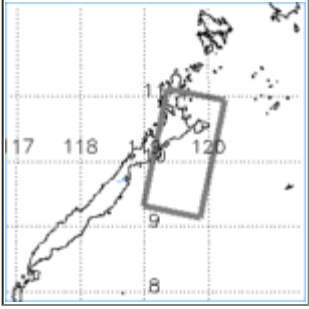
Latitude: 6° 23' S - Longitude: 104° 30' E

ERS-1 SAR image acquired over the Indian Ocean near the passage separating the Indonesian islands Sumatra and Java (Selat Sunda). A cluster of rain cells forming a common gust front is visible.
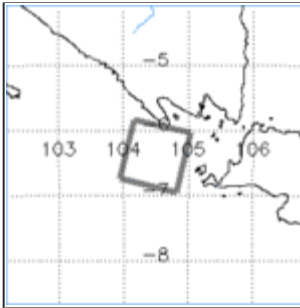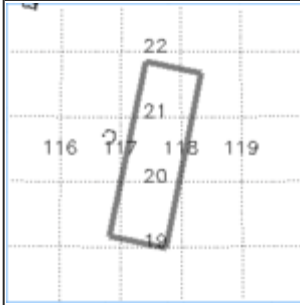

South China Sea

Latitude: 20° 26' N - Longitude: 117° 35' E

Radar signatures of rain cells of different sizes are visible on this ERS-1 SAR image of the South China Sea. The long line extending almost across the whole image from top to bottom is the radar signature of an internal solitary wave propagating eastward.

#	Orbit	Frame(s)	Satellite	Date	Time	Location
1	24684	3429	ERS-1	03-Apr-1996	12:34	
2	14408	3411	ERS-1	18-Apr-1994	03:42	
3	14408	3393	ERS-1	18-Apr-1994	03:42	
4	15975	3159-3177-3195	ERS-2	11-May-1998	02:46	
5	24320	3393-3411	ERS-2	15-Dec-1999	02:26	
6	9424	3735	ERS-1	5-May-1993	03:17	

7	21076	3177-3195-3213	ERS-1	27-Jul-1995	02:40	

References

- Atlas, D., Footprint of storms on the sea: A view from spaceborne synthetic aperture radar, *J. Geophys. Res.*, **99**, 7961-7969 (1994a).
- Atlas, D., Origin of storm footprints on the sea seen by synthetic aperture radar, *Science*, **266**, 1364-1366 (1994b).
- Atlas, D. & Black, P., The evolution of convective storms from their footprints on the sea as viewed by synthetic aperture radar from space, *Bull. Am. Meteorrol. Soc.*, **75**, 1183-1190 (1994).
- Bliven, L., Sobieski, P.W. & Craeye, C., Rain generated ring-waves: measurements and modelling for remote sensing, *Int. J. Remote Sens.*, **18**, 221-228 (1997).
- Cotton, W.R. & Anthes, R.A., Strom and cloud dynamics, *Int. Geophys. Series*, **44**, Academic Press, 880pp. (1989).
- Craeye, C., Sobieski, P.W. & Bliven, L.W., Scattering by artificial wind and rain roughned water surfaces at oblique incidences, *Int. J. Remote Sens.*, **18**, 2241-2246 (1997).
- Delrieu, G., Hucke, L. & Creutin, J.D., Attenuation in rain for X-band and C-band weather radar systems: Sensitivity with respect to the drop size distribution, *J. Appl. Meteor.*, **38**, 57-68 (1999).
- Iguchi, T., Atlas, D., Okamoto, K. & Sumi, A., Footprints of storms on the sea in the JERS-1 SAR image, *IEICE (Institute of Electronics, Information and Communication Engineers, Japan) Transactions on Comm.*, **E-78 B**, 1580-1584 (1995).
- Jameson, A.R., Li, F.K., Durden, S.L., Haddad, Z.S., Holt, B., Fogarty, T., Im, E. & Moore, R.K., SIR-C/X-SAR observations of rain storms, *Remote Sens. Environ.*, **59**, 267-279 (1997).
- Kasilingam, D., Lin, I.-I., Lim, H., Khoo, V., Alpers, W. & Lim, T.K., Investigation of tropical rain cells with ERS SAR imagery and ground-based weather radar, *Proc. 3rd ERS Symp., Space at the service of our environment, ESA publication SP-361*, v. III, 1603-1608 (1997).
- Lichtenegger, J., ERS-1 SAR images - Mirror of thunderstorms, *ESA Earth Observation Quaterly*, **53**, 7-9 (1996).
- Melsheimer, C., Alpers, W. & Gade, M., Investigation of multifrequency / multipolarization radar signatures of rain cells over the ocean using SIR-C / X-SAR data, *J. Geophys. Res.*, **103**, 18867-18884 (1998).
- Melsheimer, C., Alpers, W. & Gade, M., Simultaneous observation of rain cells over the ocean by the synthetic aperture radar aboard the ERS satellites and by surface-based weather radars, *J. Geophys. Res.*, 2000 (in press).
- Moore, R. K., Mogili, Y.S., Fang, Y., Beh, B. & Ahamad, A., Rain measurement with SIR-C/X-SAR, *Remote Sens. Environ.*, **59**, 280-293 (1997).
- Nystuen, J., A note on the attenuation of surface gravity waves by rainfall, *J. Geophys. Res.*, **95**, 18353-18355 (1990).
- Tsimplis, M., The effect of rain in calming the sea, *J. Phys. Oceanogr.*, **22**, 404-412 (1992).